2013-10-14

Investigating the effect of characteristic x-rays in cadmium zinc telluride detectors under breast computerized tomography operating conditions

Stephen J. Glick
University of Massachusetts Medical School

Et al.

Investigating the effect of characteristic x-rays in cadmium zinc telluride detectors under breast computerized tomography operating conditions

Stephen J. Glick[1] and Clay Didier[2]
[1]*Department of Radiology, University of Massachusetts Medical School, Worcester, Massachusetts 01655, USA*
[2]*enLabel Global Services, Boston, Massachusetts 02201, USA*

(Received 5 April 2013; accepted 16 August 2013; published online 10 October 2013)

A number of research groups have been investigating the use of dedicated breast computerized tomography (CT). Preliminary results have been encouraging, suggesting an improved visualization of masses on breast CT as compared to conventional mammography. Nonetheless, there are many challenges to overcome before breast CT can become a routine clinical reality. One potential improvement over current breast CT prototypes would be the use of photon counting detectors with cadmium zinc telluride (CZT) (or CdTe) semiconductor material. These detectors can operate at room temperature and provide high detection efficiency and the capability of multi-energy imaging; however, one factor in particular that limits image quality is the emission of characteristic x-rays. In this study, the degradative effects of characteristic x-rays are examined when using a CZT detector under breast CT operating conditions. Monte Carlo simulation software was used to evaluate the effect of characteristic x-rays and the detector element size on spatial and spectral resolution for a CZT detector used under breast CT operating conditions. In particular, lower kVp spectra and thinner CZT thicknesses were studied than that typically used with CZT based conventional CT detectors. In addition, the effect of characteristic x-rays on the accuracy of material decomposition in spectral CT imaging was explored. It was observed that when imaging with 50-60 kVp spectra, the x-ray transmission through CZT was very low for all detector thicknesses studied (0.5–3.0 mm), thus retaining dose efficiency. As expected, characteristic x-ray escape from the detector element of x-ray interaction increased with decreasing detector element size, approaching a 50% escape fraction for a 100 μm size detector element. The detector point spread function was observed to have only minor degradation with detector element size greater than 200 μm and lower kV settings. Characteristic x-rays produced increasing distortion in the spectral response with decreasing detector element size. If not corrected for, this caused a large bias in estimating tissue density parameters for material decomposition. It was also observed that degradation of the spectral response due to characteristic x-rays caused worsening precision in the estimation of tissue density parameters. It was observed that characteristic x-rays do cause some degradation in the spatial and spectral resolution of thin CZT detectors operating under breast CT conditions. These degradations should be manageable with careful selection of the detector element size. Even with the observed spectral distortion from characteristic x-rays, it is still possible to correctly estimate tissue parameters for material decomposition using spectral CT if accurate modeling is used. [http://dx.doi.org/10.1063/1.4821342]

I. INTRODUCTION

In an effort to improve the early stage detection and diagnosis of breast cancer, a number of research groups have been investigating the use of x-ray computerized tomography (CT) systems dedicated for use in imaging the breast.[1–7] Preliminary results suggest that dedicated breast CT systems can provide improved visualization of 3D breast tissue with similar radiation dose as compared to conventional mammography.[8,9] However, current breast CT prototypes[10,11] have limitations resulting in less than desirable spatial resolution, lesion contrast, and signal-to-noise (SNR) ratio.

We are investigating dedicated CT imaging of the breast using a direct conversion semiconductor detector that will operate in photon counting mode. For over a century now, clinical x-ray imaging detectors have operated in energy integrating mode, whereby images are formed by integrating x-ray events over a finite acquisition time. For a number of reasons, the performance of energy integrating detectors is sub-optimal for use in CT imaging of the breast. It is expected that the next generation of x-ray detectors for digital radiography and CT will have the capability of counting individually measured photons and recording their energy. Unlike x-ray detectors operating in an energy integrating mode, photon counting detectors can record and analyze each individual x-ray interacting within the detector. However, due to the high count rate typically present in x-ray CT (i.e., hundreds of millions of x-rays/s/mm^2), it has historically been impossible to operate CT detectors in a photon counting mode. Due to recent technological improvements in x-ray detectors and associated electronics, it is now becoming feasible for photon counting detectors to be used for CT applications with lower x-ray fluence requirements. Given that the dose to the breast is typically constrained to

approximately that of the dose given for mammography, one of these applications is CT breast imaging. It is estimated that the maximum flux in breast CT would be in the range of 50–150 million x-rays per mm per second.

Using direct conversion photon counting detectors for breast CT promises to provide a number of advantages over current prototypes including (1) improved spatial resolution which is critical both for detection of microcalcifications, as well as for accurately visualizing tumor borders,[12] (2) improved tumor contrast,[13] (3) reduction of detector electronic noise, (4) reduction of Swank noise,[14] (5) reduction of image lag and ghosting effects, (6) increased dynamic range, (7) improved SNR through x-ray energy weighting,[15–19] and (8) the potential for using single exposure, multiple-energy imaging to improve quantitative accuracy for contrast-enhanced CT breast imaging.[20]

The development of a semiconductor based photon counting detector for breast CT is very challenging with a number of factors contributing to the degradation of image quality including characteristic x-rays,[21] trapping, and spreading of charge as it propagates to the detector elements,[22–25] pulse-pileup,[26,27] and inhomogeneity in response between detector elements among others. Of these factors, the degradation of characteristic x-rays is an inherent phenomena in cadmium zinc telluride (CZT) that will always be present and cannot be reduced regardless of detector operating parameters (e.g., charge sharing can be reduced with increased bias voltage, pulse pileup can be reduced by lower the input flux etc.). For this reason, this study focuses on the degradation in image quality due to characteristic x-rays.

Silicon based photon counting detectors have been implemented in mammography,[28] whole-body CT,[29] and breast CT.[30] Silicon has some beneficial properties for breast CT and is insensitive to characteristic x-ray emission. However, one possible problem with silicon is a relatively low stopping power. Two promising semiconductor materials that are being studied for breast CT are cadmium telluride (CdTe) and CZT.[6,17,31–34] An interacting x-ray can produce secondary characteristic x-rays (x-ray fluorescence) with energy equivalent to the binding energies characteristic of the Cd and Te atoms. As discussed below, these characteristic x-rays can exit the semiconductor material or be re-absorbed at a misplaced location resulting in loss of spatial and energy resolution, as well as double counting of the incident x-ray. One design approach for reducing the effects of charge-sharing and characteristic x-ray reabsorption, as well as for increasing count capability is to reduce detector thickness. In addition to reduced charge trapping and spreading, a thinner detector has a number of additional benefits including reduced polarization effects, as well as a shorter electron-hole collection time, allowing for a shorter pulse.[35] Detector polarization occurs at high flux when the buildup of charge within the semiconductor becomes excessive, thereby collapsing the electric field. Bale and Szeles[36] have provided an extensive theoretical discussion of detector polarization and have shown that the maximum sustainable flux (i.e., critical flux) is inversely dependent on detector thickness. Thus, there is strong motivation for reducing the CZT detector thickness. Previous studies[21,37] have examined the effect of characteristic x-rays produced with CZT detectors of thickness 2–3 mm and kVp settings more indicative of general CT. However, breast CT typically uses lower x-ray energies than conventional CT, thus allowing the use of a thinner CZT detector without the penalty of reduced quantum efficiency. In this study, Monte Carlo simulation software is used to evaluate the effect of characteristic x-rays on spatial and spectral resolution for a CZT detector used under breast CT operating conditions. Charge sharing is not modeled, so some of the results presented here can be interpreted as an ideal upper bound on performance. Performance with typical breast CT kV spectra of 40–60 kV (Refs. 38–40) and varying CZT thicknesses (0.5–3.0 mm) are evaluated.

II. METHODS

A direct conversion, two-dimensional (2D) CZT detector operating in pulse mode was simulated. The CZT crystal was modeled with weight fractions of Cd, Te, and Zn of 40%, 55%, and 5%, respectively. Characteristic x-rays of interest can be emitted when incident x-rays interact with Cd or Te atoms, whereas interaction with the Zn atom has low probability. The average K-edge characteristic x-ray energy emitted from Cd and Te are 23.4 keV and 27.5 keV, respectively. The resulting characteristic x-rays can traverse some distance and thus can be recorded in neighboring detector elements. Figure 1 shows a number of possible outcomes for x-rays incident on the detector; (1) x-ray transmission through the CZT detector, (2) escape of characteristic x-rays into neighboring detector elements (i.e., side escape), (3) escape of characteristic x-rays out the front (towards readout electronics, referred to as front escape) or back (towards entrance, referred to as back escape), or (4) re-absorption of characteristic x-rays produced nearby and yet recorded in a detector element some distance away from the primary x-ray interaction. It should be noted that for the point spread function (PSF) studies described below, the x-ray beam was solely directed at the central detector element.

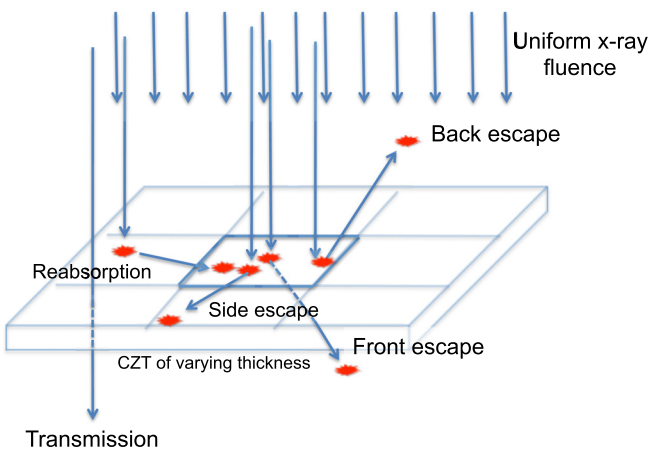

FIG. 1. An illustration showing possible outcomes from x-rays interacting within the CZT detector. (Reprinted with permission from S. J. Glick and C. S. Didier "The effect of characteristic x-rays on the spatial and spectral resolution of a CZT based detector for breast CT," in SPIE Medical Imaging **7961**, 796110 (2011). Copyright 2011 SPIE.)[54]

A. Monte Carlo simulation

The general purpose Penelope Monte Carlo simulation software[41] was used to model a parallel x-ray beam incident on a monolithic CZT crystal. CZT of varying thicknesses were simulated including 500 μm, 750 μm, 1 mm, 2 mm, and 3 mm. If not specified in the simulations discussed below, the default CZT thickness was 750 μm. An ideal pixelized detector was modeled using square detector elements of size either 0.1×0.1 mm^2, 0.2×0.2 mm^2, or 0.3×0.3 mm^2 In each simulation, the incident x-ray beam was uniformly directed normal to the detector in one of two ways; (1) over multiple detector elements or (2) at a central detector element for evaluation of the sampled point spread function (i.e., a rect function defined by the detector element size). In the latter case, neighboring detector elements were not irradiated. In all cases, the x-ray beam entered into the detector perpendicular to the detector face (it is assumed that the x-ray detector is curved so that the parallax effect will be minimized).

The Penelope code tracked all primary and characteristic x-rays (from both Cd and Te atoms) and the (x,y,z) position and energy deposited at each interaction was recorded. Electrons were not tracked. The primary x-ray interaction in the CZT over energies used for breast CT is the photoelectric effect (over 90% probable for energies up to 80 keV). The simulations assumed that no charge sharing occurred, and that each x-ray interaction contributed only to the detector element directly beneath it (i.e., electron-hole pairs migrate directly up and down from the x-ray absorption location). Simulations were conducted by tracking 100 000 x-ray histories at 1 keV intervals from 15 to 80 keV. To create simulated data for various x-ray spectra, the tungsten anode spectral model (TASMIP)[42] was used to generate normalized 50, 60, 70, and 80 kV spectra at 1 keV intervals. These normalized TASMIP x-ray spectra were then weighted by the Monte Carlo simulation results at each 1 keV interval to generate simulations for each spectra. In addition, some experiments were performed using a realistic breast CT spectrum that was obtained by modeling x-ray attenuation through a 14 cm cylinder of breast tissue composed of 50% fibroglandular tissue and 50% adipose tissue. To evaluate the attenuation resulting with varying thickness of CZT, the percentage x-ray transmission without interaction was computed.

B. Spatial resolution

To evaluate spatial resolution, a uniform x-ray fluence was directed towards the central detector element and x-ray interactions were recorded in the central detector element, as well as in neighboring detector elements. Three ideal detector element sizes were studied; 0.1×0.1 mm^2, 0.2×0.2 mm^2, and 0.3×0.3 mm^2. For most studies performed herein, all events were assumed to be recorded in the same energy bin; however, one case with binning into three energy bins was also studied.

C. Spectral resolution

To evaluate spectral resolution, the joint probability density function $h(E,E')$ was generated where E represents the incoming x-ray energy and E' represents the output x-ray energy measured by the detector. This function will be referred to herein as the energy response function. To simulate the energy response function, the incident x-ray flux was uniformly distributed over the entire detector; however, only the energy deposited within a central reference detector element was recorded. This energy deposited in the central reference detector element includes energy remaining after characteristic x-ray escape, as well as from re-absorption of characteristic x-rays generated from nearby locations. The energy response function is especially insightful for evaluating the effective spectrum in each energy bin for use in multi-energy imaging.

D. Effect of spectral resolution on accuracy of material decomposition

A common technique for material quantification with spectral CT involves parameterizing both the spatial and energy dependence of the object attenuation coefficient to be estimated.[43,44] Here, we represent the unknown object attenuation coefficient using basis functions describing the mass attenuation coefficient of adipose tissue, fibroglandular tissue, and iodine

$$\mu(E,\vec{x}) = a_1(\vec{x})f_{adi}(E) + a_2(\vec{x})f_{gla}(E) + a_3(\vec{x})f_{iod}(E), \quad (1)$$

where $a_1(\vec{x}), a_2(\vec{x}), a_3(\vec{x})$ and $f_{adi}(E), f_{gla}(E), f_{iod}(E)$ represent local density and mass attenuation coefficient for adipose tissue, fibroglandular tissue and iodine, respectively. Given this object parameterization, the expected value of the measurement λ in energy bin i at a specific detector element can be expressed as

$$\lambda_i(A_1,A_2,A_3) = \int_0^\infty B_i(E)I_0(E)D(E)\exp\left(-\sum_{J=1}^{3} f_j(E)A_j\right)dE, \quad (2)$$

where the subscript i = 1,2,3 refers to one of three energy bins, $I_o(E)$ is the blank scan energy spectra, $D(E)$ represents the energy dependent quantum efficiency of CZT, the bin sensitivity function $B_i(E)$ can be expressed as

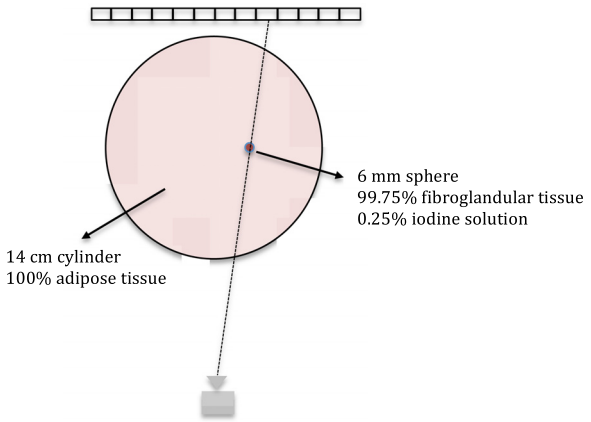

FIG. 2. Object geometry used for evaluating material decomposition.

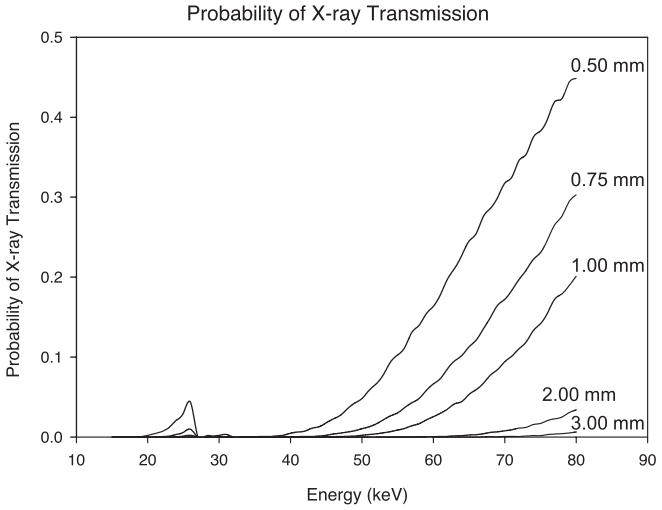

FIG. 3. Probability of x-ray transmission versus energy (monochromatic) through varying thickness of CZT. (Reprinted with permission from S. J. Glick and C. S. Didier, "The effect of characteristic x-rays on the spatial and spectral resolution of a CZT based detector for breast CT," in SPIE Medical Imaging **7961**, 796110 (2011). Copyright 2011 SPIE.)[54]

$$B_i(E) = \int_{\tau_{i-1}}^{\tau} h(E, E')dE', \tag{3}$$

and

$$A_j = \int a_j(\vec{x})dl, \quad j = 1, 2, 3. \tag{4}$$

In Eq. (3), $\{\tau_i\}$ are the threshold energies defining energy bins. To solve for the A_j's, parameter estimation methods can be used.[43,44] Here, we use the maximum-likelihood method because it is an unbiased and efficient estimator for data exhibiting a Poisson distribution. Under an assumption that the number of photons recorded in each energy bin form a set of independent Poisson random variables denoted by g_i, i = 1,2,3, then the negative log-likelihood L becomes

TABLE I. Transmission fractions for varying x-ray spectra of 50, 60, 70, and 80 kVp and varying CZT thickness of 0.5, 0.75, 1.0, 2.0, and 3.0 mm. For the most common breast CT kVp settings (highlighted in gray), transmission fraction is less than 3% for all thicknesses studied.

	CZT thickness				
	0.5 mm	0.75 mm	1.0 mm	2.0 mm	3.0 mm
50 kV	0.67%	0.08%	0.01%	0.00%	0.00%
60 kV	2.57%	0.61%	0.15%	0.00%	0.00%
70 kV	5.72%	1.95%	0.71%	0.02%	0.00%
80 kV	9.72%	4.14%	1.89%	0.12%	0.01%

$$\begin{aligned} L(g_1, g_2, g_3|A_j) &= -\ln[P(g_1, g_2, g_3|\lambda_1(A_j), \lambda_2(A_j), \lambda_3(A_j)] \\ &= \sum_{i=1}^{N}[\lambda_1(A_j) + \ln g_i\,! - g_i \ln \lambda_i(A_j)] \\ &\cong \sum_{i=1}^{N}[\lambda_1(A_j) - g_i \ln \lambda_i(A_j)]. \end{aligned} \tag{5}$$

By minimizing the above log-likelihood function, the maximum likelihood estimates A_J^{ML} can be obtained for each tissue type. The minimization can be performed using a number of different numerical algorithms, here we use the simplex method of Nelder and Mead.[45] Once the A_J^{ML} estimates are obtained, reconstructed basis images for each tissue type can be obtained by using filtered backprojection.

1. Effect of spectral resolution on the accuracy of material quantification

To explore how the degradation in spectral resolution from characteristic x-rays might affect the accuracy of material quantification in breast CT, we conducted a simple simulation study. A digital phantom was generated consisting of a small 6 mm sphere with a mixture of 997.5 mg/l of fibroglandular tissue and 2.5 mg/l of iodine solution embedded in a 12 cm diameter circular phantom of breast adipose tissue

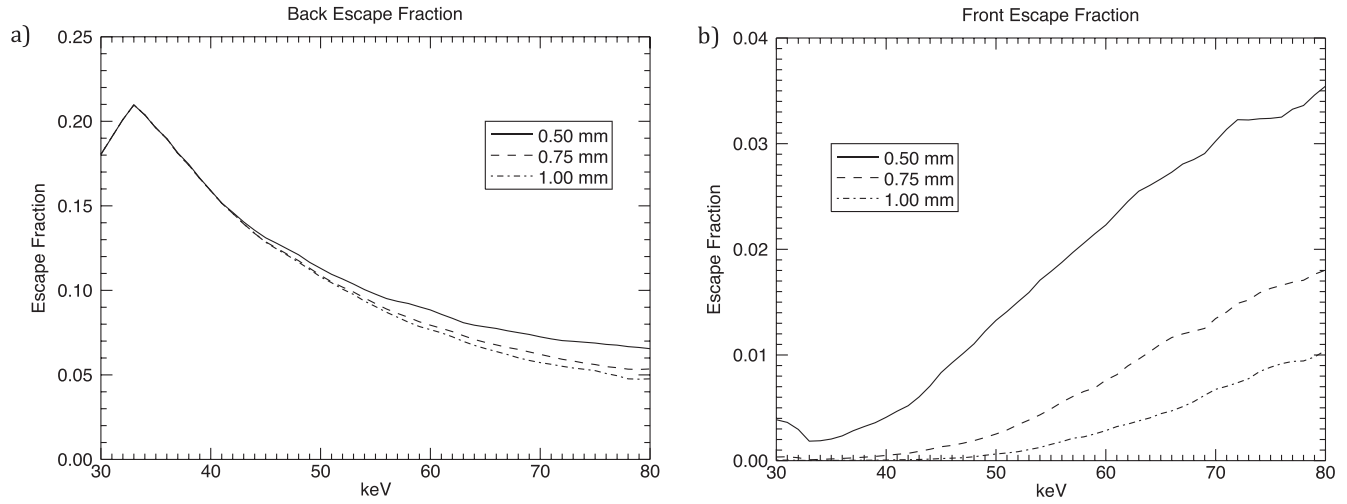

FIG. 4. Fraction of characteristic x-rays produced that escape towards; (a) the back (towards x-ray source) and (b) towards the front of the detector (where read-out electronics are located). Results are shown for three different CZT thicknesses.

(see Fig. 2). The 6 mm sphere was positioned 4 cm from the center of the circle. Equation (4) was evaluated using Siddon's ray-tracing method,[46] and the A_j line integrals for each tissue type were computed for one detector element. This line integral passed from the x-ray source to the detector element through the center of the 6 mm iodine sphere. Using Eq. (2), the mean number of detected photons was computed for three energy bins of 20–33 keV, 34–45 keV, and 46–60 keV. A 60 kV x-ray spectrum was modeled using the TASMIP developed by Boone *et al.*,[42] and the x-ray fluence of this spectrum was scaled using previously determined Monte Carlo based normalized glandular dose coefficients[47] to provide a 10 mGy mean glandular dose to the breast-like phantom over 360 projection angles. The energy dependent linear attenuation coefficients of the adipose and fibroglandular tissue were modeled based on the previous experimental tissue measurements by Johns and Yaffe,[48] and the coefficients for iodine were taken from the NIST website.[49] An ensemble of 1000 noisy measurements (g_i) was produced by selecting a random deviate from a Poisson distribution with mean of $\lambda_{i.}$ The maximum-likelihood algorithm was then applied using the simplex method, and 1000 estimates of A_J^{ML} for each tissue type were computed.

III. RESULTS

A. Attenuation properties of CZT

Figure 3 shows the probability of mono-energetic x-rays passing without interaction through a CZT detector of various thicknesses ranging from 0.5 mm to 3.0 mm. For typical breast CT x-ray energies (i.e., less than 60 keV), it is observed that the probability of x-ray transmission is less than 15% for all the CZT thicknesses studied. Table I shows transmission fractions for varying x-ray spectra of 50, 60, 70, and 80 kVp modeled with a tungsten anode x-ray tube using 2 mm Al filtering. These spectra have also been modeled as passing through a 14 cm diameter breast of composition 50% adipose tissue and 50% fibroglandular tissue. It is observed from Table I that the probability of x-ray transmission is less than 10% for all spectra and thicknesses studied.

B. Characteristic X-ray escape

Figure 4 shows the fraction of all characteristic x-rays produced that escape out towards the back (i.e., towards the x-ray source) of the detector, as well as towards the front of the detector (i.e., where the read-out electronics are located).

TABLE II. Percentage of characteristic x-rays produced that escape from the front of detector (towards detector pixels).

	Front escape		
	0.5 mm	0.75 mm	1.0 mm
50 kV	0.4%	0.1%	0.0%
60 kV	0.8%	0.1%	0.0%
70 kV	1.1%	0.3%	0.1%
80 kV	1.5%	0.3%	0.2%

TABLE III. Percentage of characteristic x-rays produced that escape from the back of the detector (towards side of x-ray entrance).

	Back escape		
	0.5 mm	0.75 mm	1.0 mm
50 kV	16.7%	16.7%	16.7%
60 kV	14.7%	14.5%	14.5%
70 kV	13.2%	12.9%	12.8%
80 kV	12.0%	11.5%	11.4%

Shown are results for three different values of detector thickness, 0.5 mm, 0.75 mm, and 1.0 mm. From Fig. 4(a), it is observed that the back escape fraction increases slightly at low energy and then decreases with increasing energy. The back escape fraction can be as high as 0.22 at lower energies. There was little variation in back escape fraction observed with changes in detector thickness. The front escape fraction was observed to be low at all thicknesses with a maximum value of less than 0.04; however, a relatively large change in front escape fraction was observed with varying CZT thickness (see Fig. 4(b)). Tables II and III show front and back escape fractions for varying x-ray spectra of 50, 60, 70, and 80 kVp modeled with a tungsten anode x-ray tube using 2 mm Al filtering and passing through a 14 cm diameter breast of composition 50% adipose tissue and 50% fibroglandular tissue. Results are shown for three values of CZT thickness, 0.5 mm, 0.75 mm, and 1.0 mm. It is observed that the front escape fractions for all spectra are very small, less than 0.02. The back escape fraction ranged from 0.114 to 0.167 over all spectra, suggesting that many more characteristic x-rays generated escape out the back of the detector rather than the front.

Figure 5 shows the fraction of characteristic x-rays produced that escape from the irradiated detector element out the side to another neighboring detector element. Side escape fractions are shown as a function of energy (keV) for three different detector element sizes, 0.1 mm, 0.2 mm, and 0.3 mm. As expected, the side escape fraction increases with

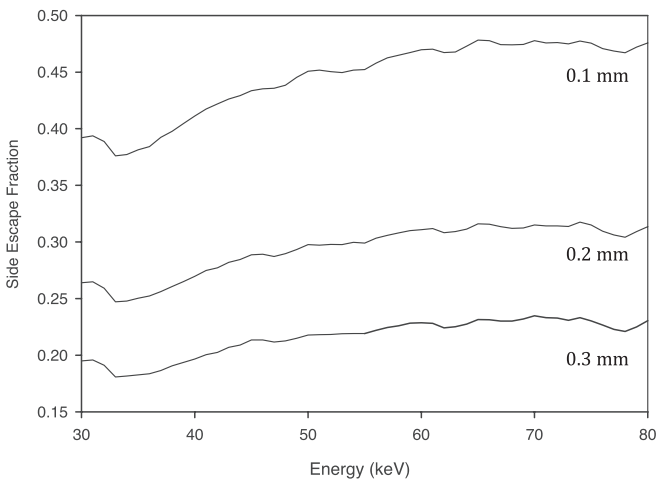

FIG. 5. Fraction of characteristic x-rays produced that escape from the irradiated pixel out the side to another neighboring pixel. Results are shown for three different pixel sizes.

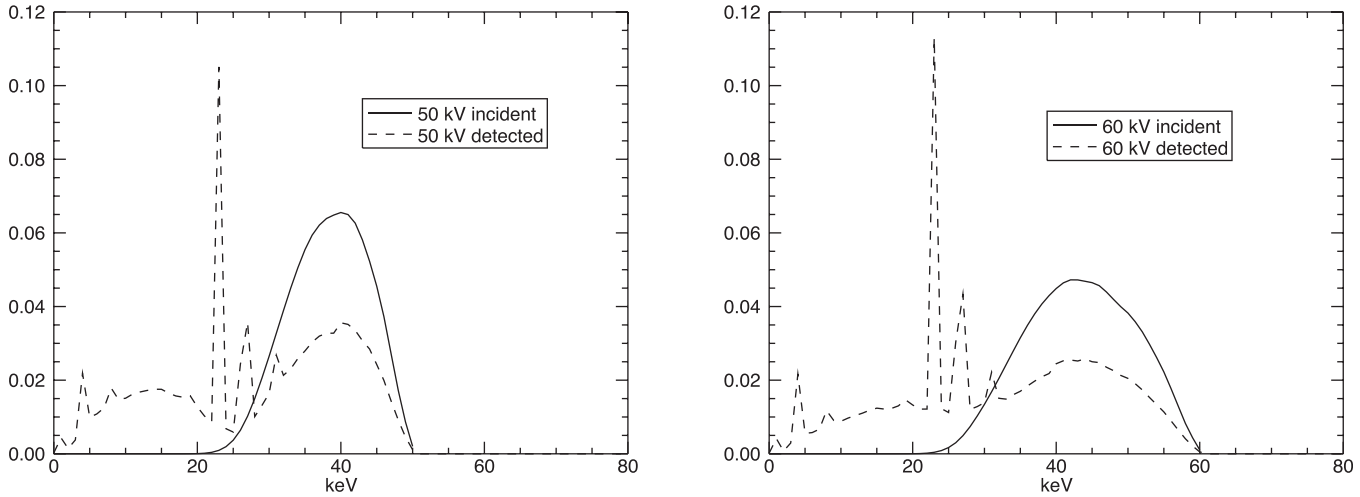

FIG. 6. X-ray spectra incident on the detector after exiting a 14 cm breast with 50% adipose tissue and 50% fibroglandular tissue (solid line) and that absorbed by the detector (dashed line) for (a) 50 kV and (b) 60 kV

decreasing detector element size. For example at 40 keV, side escape fraction of 0.42, 0.27, and 0.20 was observed for detector element size of 0.1 mm, 0.2 mm, and 0.3 mm, respectively. The biggest jump in side escape fraction was observed in going from 0.2 mm to 0.1 mm detector element size. The side escape fraction was observed to have a slight energy dependence, increasing with increasing energy from 35 to 80 keV.

Escape and reabsorbed characteristic x-rays can severely distort the recorded energy x-ray spectra. Shown in Fig. 6 are 50 kV (a) and 60 kV (b) spectra incident on the detector after passing through 14 cm of breast tissue of composition

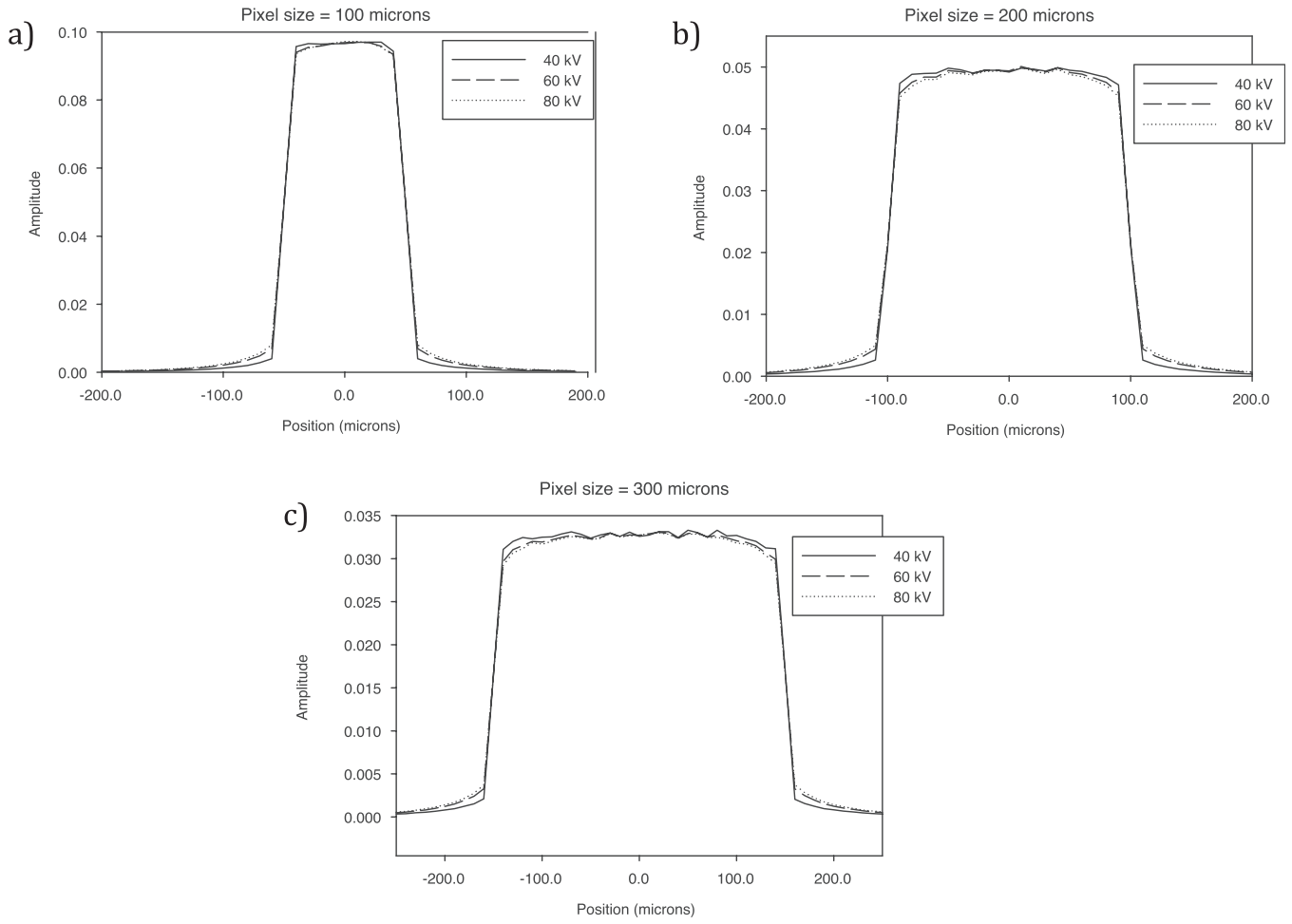

FIG. 7. Shown are profiles through simulated PSFs before pixel sampling, where the x-ray beam irradiates an area of (a) 0.1 mm^2, (b) 0.2 mm^2, and (c) 0.3 mm^2. Results are shown for 40 kV, 60 kV, and 80 kV spectra.

50% adipose and 50% fibroglandular, as well as spectra that are absorbed by the detector. These spectra were recorded from the central detector element when the whole detector was irradiated. More discussion on energy spectrum distortion is given in Sec. III D below.

C. PSF

Fig. 7 shows PSFs before pixel sampling (the PSF is actually sampled on a 10 μm^2 grid), where the x-ray beam irradiates areas of three sizes, (a) 0.1 mm^2, (b) 0.2 mm^2, and (c) 0.3 mm^2. Fig. 8 shows normalized point spread functions after pixel sampling when the x-ray beam irradiates the central detector element of a 5×5 detector element array. Shown are PSFs for three detector elements sizes, (a) 0.1 mm, (b) 0.2 mm, and (c) 0.3 mm simulated with three different kV spectra; 40 kV (1st column), 60 kV (2nd column), and 80 kV (3rd column). Also shown is the amplitude of the central detector element. Deviations from the ideal detector element aperture (i.e., all events recorded in the central detector element, and PSF with amplitude of 1.0) are due to emission of characteristic x-rays that are reabsorbed in neighboring detector elements. For all PSFs shown in Fig. 8, the number of events in each of the 3×3 detector elements was greater than 10 000. Thus at a minimum, the fractional standard deviation (FSD) (standard deviation/mean) was 1%, but most detector elements had a FSD of much lower.

It is important to keep in mind that these results assume one large energy bin. Since photon counting detectors allow for the use of multiple energy bins, a higher energy bin would contain less characteristic x-ray reabsorption. Fig. 9 also shows normalized PSFs after pixel sampling when the

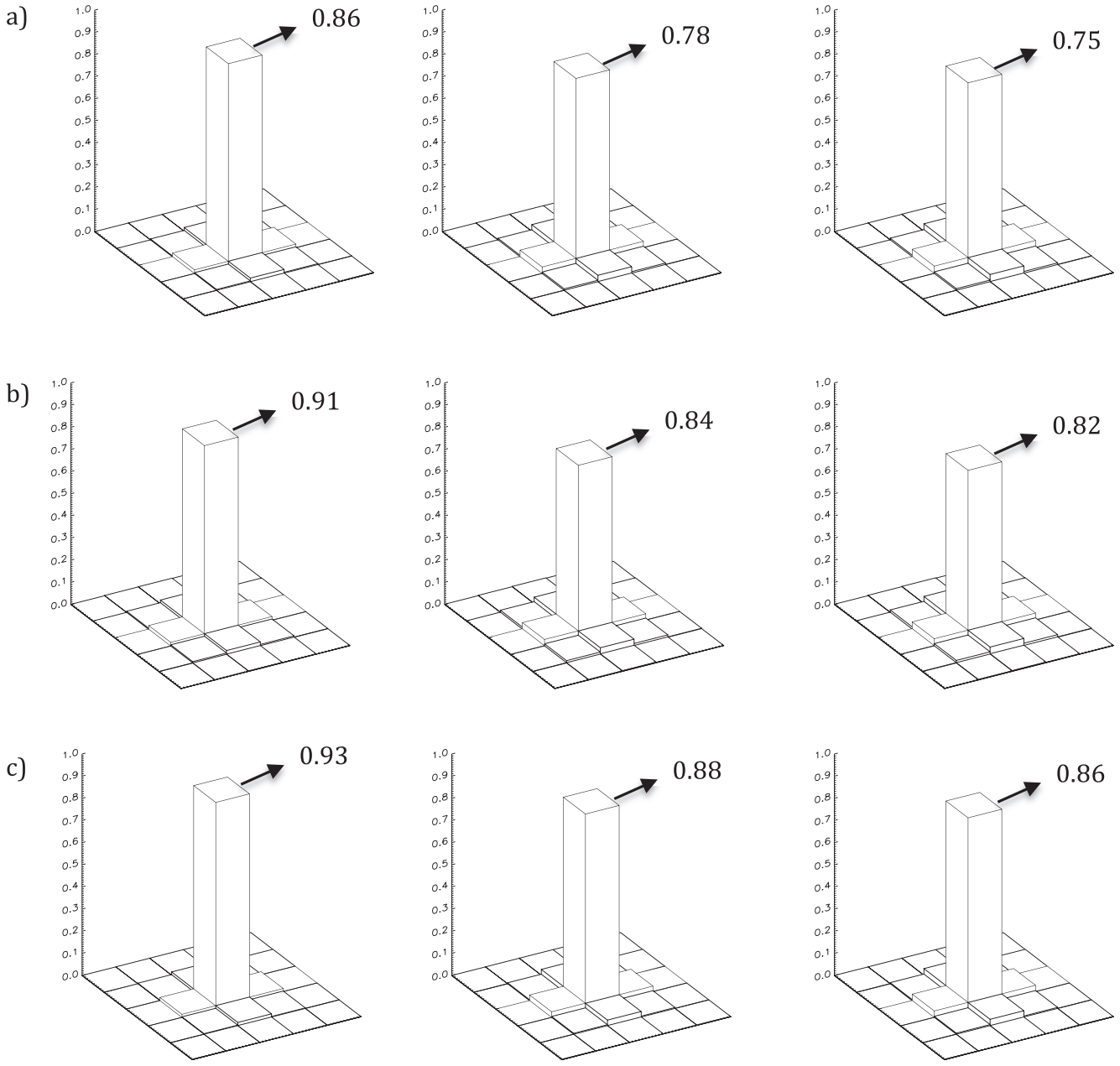

FIG. 8. Shown are normalized PSFs after pixel sampling, where the x-ray beam irradiates the central detector element of a 5×5 detector element array. Rows (a), (b), and (c) show PSFs with 0.1, 0.2, and 0.3 mm detector elements, with columns showing PSFs simulated at 40, 60, and 80 kV.

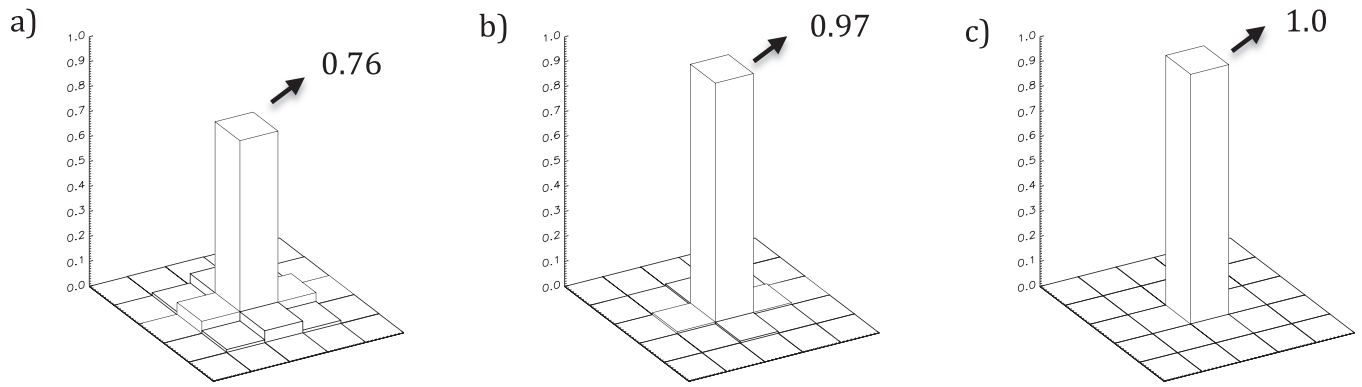

FIG. 9. Shown are normalized PSFs after pixel sampling, where the x-ray beam irradiates the central detector element of a 5 × 5 detector element array. PSFs for three energy bins are shown; (a) 15–30 keV, (b) 31–45 keV, and (c) 46–60 keV.

x-ray beam irradiates the central detector element of a 5 × 5 detector array; however, x-rays are binned into three energy windows, 15–30 keV, 31–45 keV, and 46–60 keV. It is observed that the lower energy window has substantially more degradation of the PSF.

D. Energy response function

The energy response function, $h(E, E')$, for a 0.2 mm detector element size is shown in Figure 10. The abscissa of Fig. 10 represents the incident x-ray energy (E), and the ordinate represents the measured x-ray energy (E'). This 2D function was generated by recording all energy interactions within a central reference detector element for an incident x-ray beam that irradiated the entire detector array. An approximate model of energy resolution was implemented by blurring the recorded energy with a Gaussian function with $\sigma = 0.85$ keV. The diagonal line in the energy response function represents the photopeak, or all x-rays that deposit all of their energy into the reference detector element. Also observed are a number of horizontal lines approximately below 32 keV. These lines represent characteristic x-rays

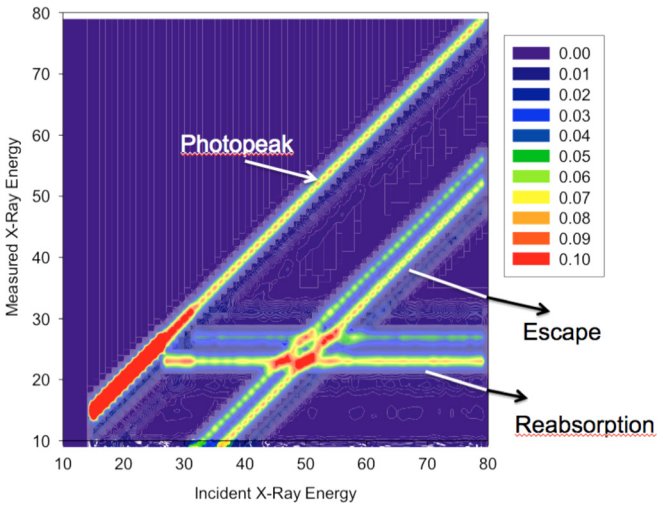

FIG. 10. The energy response function for a 0.2 mm detector element size. The color levels the fraction of occurrence. (Reprinted with permission from S. J. Glick and C. S. Didier, "The effect of characteristic x-rays on the spatial and spectral resolution of a CZT based detector for breast CT," in SPIE Medical Imaging **7961**, 796110 (2011). Copyright 2011 SPIE.)[54]

generated in neighboring detector elements that have been reabsorbed in the central reference detector element. The diagonal lines parallel to the photopeak diagonal line are due to characteristic x-ray escape, leaving partial energy absorbed within the reference detector element. Figure 11 shows energy response functions for 0.1 mm and 0.3 mm detector element size. Fig. 12 shows profiles though the energy response function (along the dashed vertical line in Fig. 11) for a monochromatic incident energy of 70 keV. It can be observed that the amplitude of the photopeak (spectra around 70 keV) is lower for the 0.1 mm detector element case than the 0.3 mm case. This is because there is higher probability of x-ray escape and reabsorption for the smaller detector element. This is also observed in the profiles showing higher probability at the 23 keV (from reabsorption) and 43 keV (from escape) peaks for the 0.1 mm detector element as compared to the 0.3 mm detector element.

Fig. 13 illustrates how the energy response function, $h(E, E')$, can be used to gain insight into the performance of dual-energy imaging. Consider the case of using a 60 kV spectra for dual energy breast CT imaging with one window ranging from 22 to 40 keV, and the other one from 40 to 60 keV. Then the two quadrants located along the diagonal in Fig. 12 would represent regions where x-rays are assigned a correct energy, whereas the quadrant located in the bottom right of the figure would represent a region where x-rays are assigned an incorrect energy. Thus, it can be observed that x-ray escape and characteristic x-ray re-absorption contribute largely to the incorrectly assigned region.

Shown in Fig. 14 is the input 60 kV spectrum (shaded gray), along with bin sensitivity functions ($B_i(E)$, i = 1,2, see Eq. (3)) for the lower (22–40 keV) and higher (40–60 keV) energy windows. The overlap between the two bin sensitivity functions is 48.6% and is indicated by the cross-hatch markings. This level of overlap is comparable to that present in dual source CT, and will penalize the accuracy of material decomposition if not corrected for. As observed in Fig. 13, characteristic x-ray re-absorption below approximately 30 keV contributes largely due to the overlap of bin sensitivity functions.

One possible remedy for this overlap is to raise the lower energy threshold. For example, Fig. 15 shows bin sensitivity functions for a lower energy window of 31–40 keV

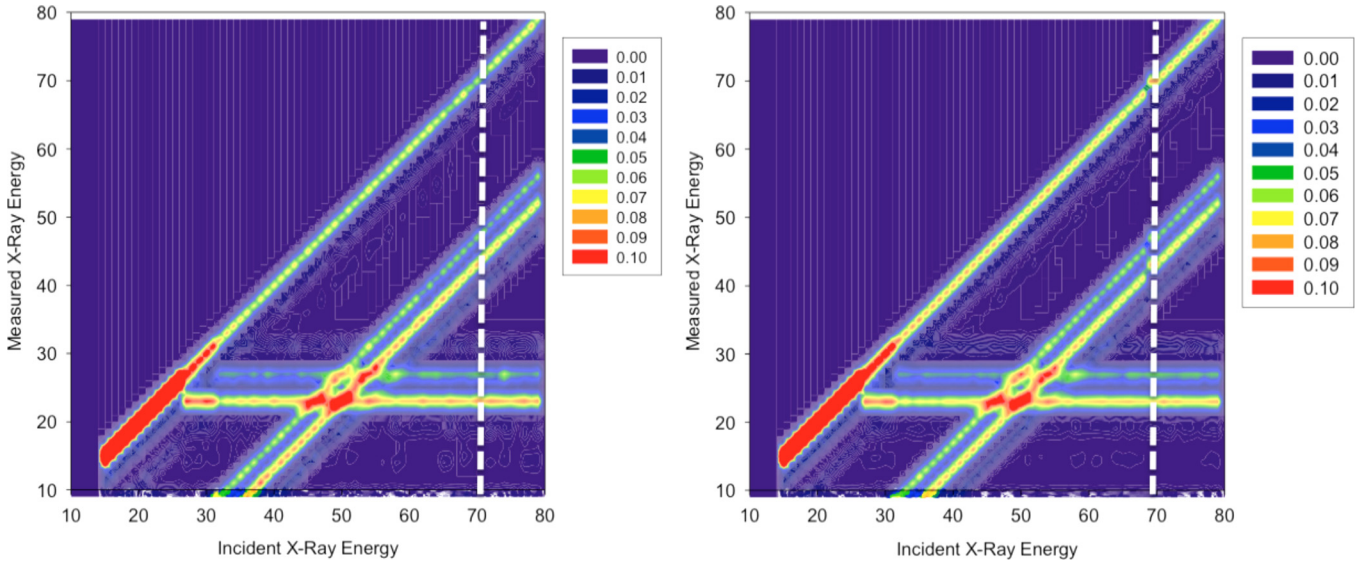

FIG. 11. The energy response functions for 0.1 mm detector element size (left) and 0.3 mm detector element size (right). Profiles through the energy response as indicated by dashed line are shown in Figure 11. The color levels represent the fraction of occurrence.

and an upper energy window of 40–60 keV. Raising the lower energy threshold to 31 keV results in a decrease in overlap from 48.6% to 17.7%. However, there is some useful information contained within x-rays lower than 31 keV, and eliminating this information could increase noise and reduce performance.

E. Effect of spectral resolution on the accuracy of material quantification

To evaluate the reduction in material quantification accuracy due to characteristic x-rays, A_J^{ML}'s were estimated with and without using an accurate model of the bin sensitivity function $B_i(E)$ for the case of a detector with detector element size of 0.2 mm. In all cases, the true values of A_1, A_2, and A_3 (i.e., line integrals for adipose tissue, fibroglandular tissue, and iodine) were 67.33, 0.68, and 6.55 pixels, respectively. Shown in Fig. 16 are two distributions (1000 samples) for estimated parameters of A_1 (adipose tissue) plotted versus A_3 (iodine). The distribution shown in the top right corner is that obtained when incorrectly assuming no spectral blurring (i.e., assuming no characteristic x-rays) in computing the ML estimates and the distribution on the bottom left is that obtained when assuming perfect knowledge of the bin sensitivity function. It can be observed that in the former case, a very large bias is observed; however, when assuming the bin sensitivity function is known, the estimation bias is very small. This suggests that if an accurate model of the bin sensitivity function can be determined, then accurate low-bias estimates of A_j can be computed.

Fig. 17 shows the distribution of estimated parameters A_1 (adipose tissue) versus A_3 (iodine) for three different detector element sizes, 0.1 mm, 0.2 mm, and 0.3 mm. In each

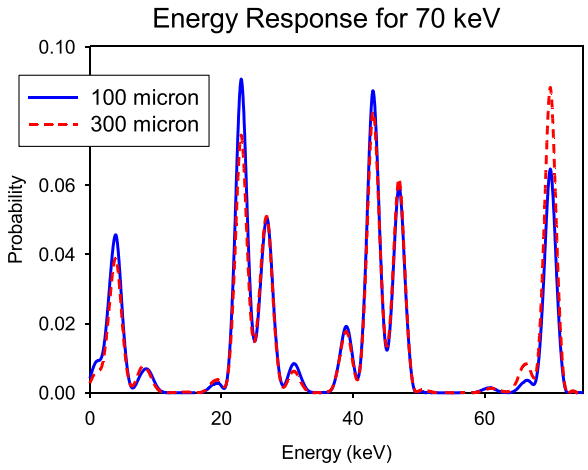

FIG. 12. Profiles through the energy response functions shown in Fig. 9 through the indicated dashed line.

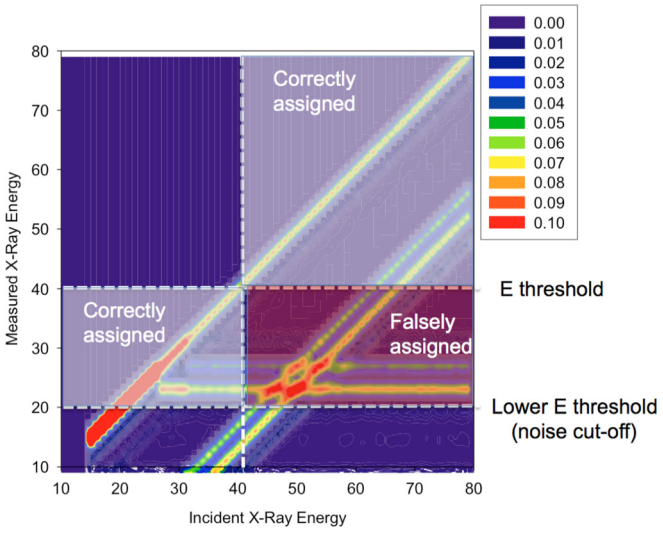

FIG. 13. Illustration demonstrating how the energy response function can be used to gain insight into dual-energy imaging performance. The two quadrants located along the diagonal indicate regions where the x-ray energy is correctly assigned. The quadrant indicated as "falsely assigned" shows a region where characteristic x-rays emission causes an incorrect energy measurement.

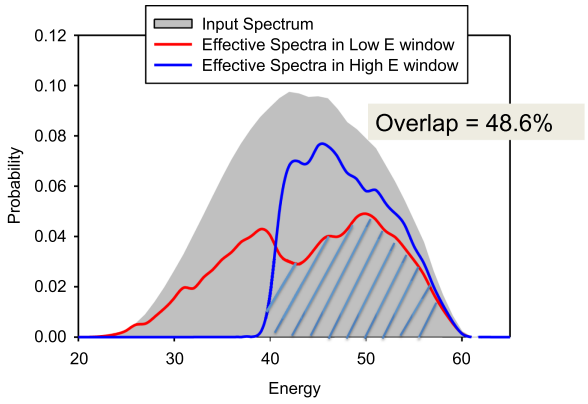

FIG. 14. 60 kV input spectra (shown in gray) and system weighting functions for the lower (22–40 keV) and higher (40–60 keV) energy windows. The overlap (shown by cross-hatch markings) is 48.6%.

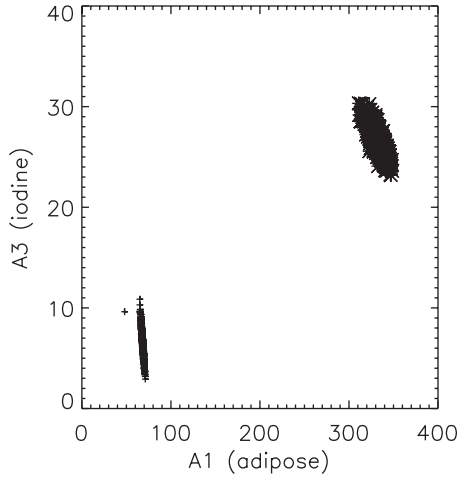

FIG. 16. Statistical distributions of estimated parameters A_1 (adipose) versus A_3 (iodine). The distribution on the top right is that obtained when incorrectly assuming no spectral blurring (i.e., no characteristic x-rays) in computing the ML estimates and the distribution on the bottom left is that obtained when assuming perfect knowledge of the bin sensitivity function.

case, the ML estimates were computed with perfect knowledge of the bin sensitivity function ($B_i(E)$). It can be observed that the bias in each case is very small; however, the estimator variance increases with decreasing detector element size. The fractional standard deviation (i.e., standard deviation/mean) for 0.1 mm, 0.2 mm, and 0.3 mm detector element sizes was 0.024, 0.017, and 0.010 and 0.230, 0.184, and 0.128, respectively, for parameters A_1 (adipose tissue) and A_3 (iodine). Also note that a negative correlation between A_1 and A_3 is observed.

IV. DISCUSSION

One of the goals of this study was to investigate whether the thickness of a CZT detector used for breast CT could be reduced from the 2–3 mm of previously reported detectors studied for breast CT[17,50] without significant penalty. Fig. 3 shows that for monochromatic energies less than 50 keV (predominant energy range for breast CT), the probability of x-ray transmission for all thicknesses tested is less than 6%. Furthermore, Table I shows that for 50 kV and 60 kV spectra

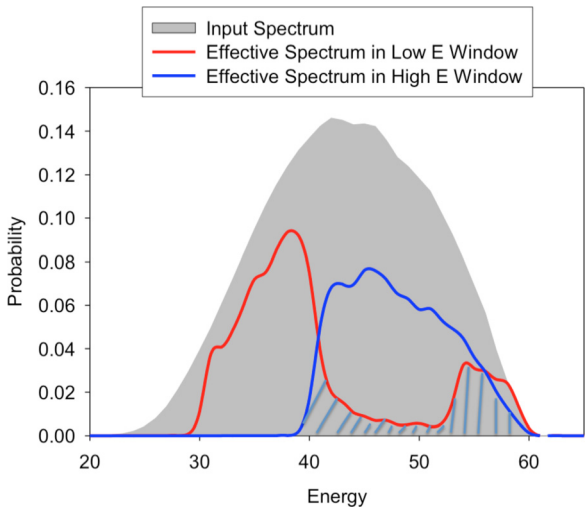

FIG. 15. 60 kV input spectra (shown in gray) and system weighting functions for lower (31–40 keV) and higher (40–60 keV) energy windows. The overlap (shown by cross-hatch markings) is 17.7%.

typically used in breast CT, the probability of x-ray transmission through the detector is less than 3%, even with the smallest 0.5 mm thick detector. These data suggest that CZT thickness can be reduced without an excessive penalty in quantum efficiency.

Characteristic x-rays produced within the CZT can escape the detector exiting through the back side (towards the x-ray source), or through the front side (towards the read-out electronics). These escape x-rays are problematic in that only part of the primary x-ray energy is absorbed thus degrading spectral resolution. Figure 4 and Tables II and III clearly illustrate that most of the escape characteristic x-rays exit out the back side of the detector, and that the probability of back side escape varies little with CZT thickness. This is because it is more likely for primary x-rays to be absorbed near the entrance to the detector. Consequently, decreasing the detector thickness from 2.0–3.0 mm to 0.5–1.0 mm does not significantly effect the fraction of escape photons.

Characteristic x-rays can also be re-absorbed in neighboring detector elements, and Fig. 5 shows that this is substantially more likely with decreasing detector element size. Of all x-rays interacting by photoelectric effect in Cd and Te atoms, 80% occur at the K-shell and 20% occur at the L-shell.[51] Of the 80% K-shell interactions, 87% of these yield characteristic x-rays, whereas 13% yield Auger electrons.[52] Thus, approximately 70% of x-rays interacting by photoelectric effect in the CZT material will produce K-shell characteristic x-rays. With a detector element size of 0.1 mm, between 40% and 50% of characteristic x-rays produced escape from the irradiated detector element to a neighboring detector element, whereas a significant reduction in side escape fraction is observed with detector elements of size 0.2 mm and 0.3 mm. More insight into the effect of side escape x-rays can be observed in the PSFs of Fig. 8. For the worst case scenario of imaging with an 80 kV spectrum and using a detector with element size of 0.1 mm, 25% of characteristic x-rays will spread to

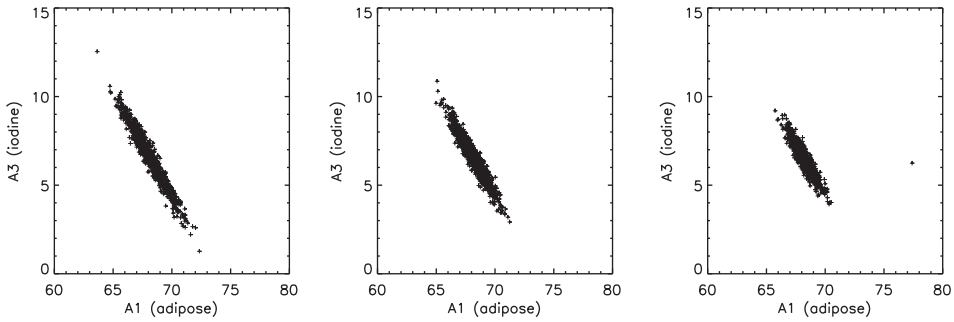

FIG. 17. The distribution of estimated parameters A_1 (adipose tissue) versus A_3 (iodine) for three different detector element sizes; (a) 0.1 mm, (b) 0.2 mm, and (c) 0.3 mm.

neighboring detector elements. However, it is observed that PSF blurring is reduced with lower kV spectra and use of detectors with bigger detector elements. Only 9% of x-rays will spread to neighboring detector elements with a 40 kV spectra and a detector element size of 0.2 mm. Further studies are needed to evaluate the effect of this spatial resolution loss on breast CT task performance; however, the PSF blur observed here is less than that observed in indirect conversion detectors currently used in prototype breast CT scanners. It should also be noted that the PSFs shown in Fig. 8 are simulated for one large energy bin encompassing all x-ray energies. Fig. 9 shows that if multiple energy bins are used, the PSF blur will only be evident in lower energy windows (<32 keV). From these observations, it can be concluded that degradation of the PSF due to characteristic x-rays will probably not be a major limitation for CZT based breast CT detectors.

When using photon counting detectors with multiple energy bins for dual- or multiple energy CT, characteristic x-rays cause higher energy incident x-rays to be erroneously recorded into lower energy bins creating a non-ideal bin sensitivity function, $B_i(E)$ (see Figs. 10–12). As observed in Eq. (5), ML estimation of the unknown material parameters requires an estimate of the expected value of the measurement in bin i (i.e., λ_i). From Eq. (2), the evaluation of this expression requires an accurate estimate of the bin sensitivity function $B_i(E)$. Results shown in Fig. 16, as well as other simulation results (not shown) suggest that if $B_i(E)$ is known (or can be accurately estimated), then unbiased estimates of the tissue parameters can be computed. This is not surprising because the ML estimator from Poisson distributed data is unbiased and efficient.

However, if it is incorrectly assumed that $B_i(E)$ is ideal (i.e., no degradation in spectral resolution), then a large bias in parameter estimation is observed (e.g., see Fig. 16). In other words, accurate modeling of the bin sensitivity function is necessary for accurate performance in spectral breast CT. There have been a few reports discussing useful methods for modeling of the bin sensitivity function. Schlomka *et al.*[44] have modeled $B_i(E)$ by measuring the response at monochromatic energies using a synchrotron, whereas Schmidt[53] have used a calibration method that acquires measurements through materials with known thickness.

Although unbiased tissue parameter estimates are achievable with accurate modeling of $B_i(E)$, the results presented in Fig. 17 show that the variance of parameter estimates for adipose tissue and iodine is affected by the detector element size. Since Figs. 10–12 show that degradation of the bin sensitivity function increases with decreasing size of the detector element, one can thus infer that escape and reabsorbed characteristic x-rays increase the variance of tissue parameter estimates.

V. CONCLUSIONS

A number of conclusions can be made from this study. First, it should be possible to reduce the thickness of CZT in breast CT detectors to below 1 mm as compared to 2–3 mm used in previous studies[17,50] without a significant reduction in detector quantum efficiency. Reducing CZT thickness will provide a number of benefits including reduced charge trapping, and an increase in usable flux before polarization effects degrade count-rate performance.[36] CZT thickness can be reduced to 0.5–1.0 mm and still transmit less than 3% of x-rays for 50–60 kV spectra.

Second, although characteristic x-ray escape can degrade the PSF, this blurring is small if the detector element is 0.2 mm or greater. Furthermore, with multiple energy bins, the PSF blur due to characteristic x-rays will only be present for the lower energy window. Although this degradation in spatial resolution appears to be small, further studies are needed to assess the PSF degradation on breast CT task performance. Finally, it was observed that the escape and reabsorption of characteristic x-rays can degrade spectral resolution, especially as the size of the detector element is decreased. This spectral degradation can potentially affect the accuracy in spectral CT material decomposition algorithms. However, if an accurate estimate of the bin sensitivity function can be obtained (either through a calibration measurement or through simulation), then low bias estimation of the unknown tissue parameters can be achieved by using a maximum likelihood objective function.

One limitation of this study is that charge sharing is not modeled; therefore, the results presented here should be interpreted as an ideal upper bound on performance. It is expected that if the charge sharing effects could be accurately modeled, then the maximum likelihood method would still achieve accurate low bias estimates of the tissue parameters as demonstrated herein, since the maximum likelihood method is an unbiased estimator.

In summary, it appears as if the effects of characteristic x-rays will not be a limitation in CZT detector based breast spectral CT. Future studies will determine if the addition of charge sharing into the simulation will change this conclusion.

ACKNOWLEDGMENTS

This work was supported in part by the National Institutes of Health (NIH) under Grant No. R01 CA140400 from the National Cancer Institute, and a research grant from Toshiba Medical Research Institute (TMRI). Its contents are solely the responsibility of the authors and do not necessarily represent the official views of NIH or TMRI.

[1]J. M. Boone, T. R. Nelson, K. K. Lindfors, and J. A. Seibert, "Dedicated breast CT: Radiation dose and image quality evaluation," Radiology **221**, 657–677 (2001).
[2]S. J. Glick, "Breast CT," Annu. Rev. Biomed. Eng. **9**, 501–526 (2007).
[3]R. Ning, Y. Yu, D. Conover, X. Lu, H. He, Z. Chen, L. Schiffhauer, and J. Cullinan, "Preliminary system characterization of flat panel detector-based cone-beam CT for breast imaging," Proc. SPIE **5368**, 292–303 (2004).
[4]M. P. Tornai, R. L. McKinley, C. N. Bryzmialkiewicz, P. Madhav, S. J. Cutler, D. J. Crotty, J. E. Bowsher, E. Samei, and C. E. Floyd, "Design and development of a fully-3D dedicated x-ray computed mammotomography system," Proc. SPIE **5745**, Medical Imaging 2005: Physics of Medical Imagaging, 189 (2005).
[5]B. Chen and R. Ning, "Cone-beam volume CT breast imaging: Feasibility study," Med. Phys. **29**, 755–770 (2002).
[6]W. A. Kalender, M. Beister, J. M. Boone, D. Kolditz, S. V. Vollmar, and M. C. Weigel, "High-resolution spiral CT of the breast at very low dose: Concept and feasibility considerations," Eur. Radiol. **22**, 1–8 (2012).
[7]L. Chen, C. C. Shaw, S. Tu, and T. Wang, "Cone-beam CT breast imaging with a flat-panel detector: A simulation study," Proc. SPIE **5745**, Medical Imaging 2005: Physics of Medical Imaging, 943 (2005).
[8]K. K. Lindfors, J. M. Boone, R. S. Nelson, K. Yang, A. L. C. Kwan, and D. W. Miller, "Dedicated breast CT: Initial clinical experience," Radiology **246**, 725–733 (2008).
[9]A. O'Connell, D. L. Conover, Y. Zhang, P. Seifert *et al.*, "Cone-beam CT for breast imaging: Radiation dose, breast coverage, and image quality," AJR, Am. J. Roentgenol. **195**, 496–509 (2010).
[10]A. L. C. Kwan, J. M. Boone, K. Yang, and S-Y. Huang, "Evaluation of the spatial resolution characteristics of a cone-beam breast CT scanner," Med. Phys. **34**, 275–281 (2007).
[11]T. Gilat-Schmidt, "Dedicated Breast CT: Current status and new directions," Curr. Med. Imag. Reviews **6**, 61–71 (2010).
[12]J. Rowlands and J. Yorkston, "Flat panel detectors for digital radiography," in *Handbook of Medical Imaging: Volume 1. Physics and Psychophysics*, edited by J. Beutel, H. Kundel, and R. VAn Metter (SPIE Press, Bellingham, WA, 2000), pp. 223–314.
[13]S. Kappler, D. Niederlohner, K. Stierstofer, and T. Flohr, "Contrast-enhancement, image noise, and dual-energy simulations for quantum-counting clinical CT," in *SPIE Medical Imaging* (San Diego, CA, 2010), Vol. 7622.
[14]R. Swank, "Absorption and noise in x-ray phosphors," J. Appl. Phys. **44**, 4199–4203 (1973).
[15]T. G. Schmidt, "Optimal 'image-based' weighting for energy-resolved CT," Med. Phys. **36**, 3018–3027 (2009).
[16]T. G. Schmidt, "CT energy weighting in the presence of scatter and limited energy resolution," Med. Phys. **37**, 1056–1067 (2010).
[17]H. Le, J. Ducote, and S. Molloi, "Radiation dose reduction using a CdZnTe-based computed tomography system: Comparison to flat-panel detectors," Med. Phys. **37**, 1225–1236 (2010).
[18]P. M. Shikhaliev, "The upper limits of the SNR in radiography and CT with polyenergetic x-rays," Phys. Med. Biol. **55**, 5317–5339 (2010).
[19]K. S. Kalluri, M. Mahd, and S. J. Glick, "Investigation of energy weighting using an energy discriminating photon counting detector for breast CT," Med. Phys. **40**, 081923 (2013).
[20]B. Zhao, H. Gao, H. Ding, and S. Molloi, "Tight-frame based iterative image reconstruction for spectral breast CT," Med. Phys. **40**, 1–10 (2013).
[21]P. M. Shikhaliev, S. G. Fritz, and J. W. Chapman, "Photon counting multi-energy x-ray imaging: Effect of the characteristic x-rays on detector performance," Med. Phys. **36**, 5107–5119 (2009).
[22]M. E. Myronakis and D. G. Darambara, "Monte Carlo investigation of charge-transport effects on energy resolution and detection efficiency of pixelated CZT detectors for SPECT/PET applications," Med. Phys. **38**, 455–467 (2011).
[23]H. H. Barrett and K. J. Myers, *Foundations of Image Science* (John Wiley, 2003).
[24]G. Pellegrini, M. Maiorino, G. Blanchot, M. Chmeissani, J. Garcia, M. Lozano, R. Martinez, C. Puigdengoles, and M. Ullan, "Direct charge sharing observation in single-photon-counting pixel detector," Nucl. Instrum. Methods Phys. Res. A **573**, 137–140 (2007).
[25]E. Gros d'Aillon, J. Tabary, A. Gliere, and L. Verger, "Charge sharing on monolithic CdZnTe gamma-ray detectors: A simulation study," Nucl. Instrum. Methods Phys. Res. A **563**, 124–127 (2006).
[26]K. Taguchi, E. C. Frey, X. Wang, J. S. Iwanczyk, and W. C. Barber, "An analytical model of the effects of pulse pileup on the energy spectrum recorded by energy resolved photon counting x-ray detectors," Med. Phys. **37**, 3957 (2010).
[27]K. Taguchi, M. Zhang, E. C. Frey, X. Wang, J. S. Iwanczyk, E. Nygard, N. E. Hartsough, B. M. Tsui, and W. C. Barber, "Modeling the performance of a photon counting x-ray detector for CT: Energy response and pulse pileup effects," Med. Phys. **38**, 1089 (2011).
[28]M. Aslund, B. Cederstrom, M. Lundqvist, and M. Danielsson, "Physical characterization of a scanning photon counting digital mammography system based on Si-strip detectors," Med. Phys. **34**, 1918–1925 (2007).
[29]H. Bornefalk and M. Danielsson, "Photon-counting spectral computed tomography using silicon strip detectors: A feasibility study," Phys. Med. Biol. **55**, 1999–2022 (2010).
[30]J. Iwanczyk, E. Nygard, J. Wessel, N. Malakhov, G. Wawrzyniak, N. Hartsough, T. Gandhi, and W. Barber, "Breast CT using a silicon photon counting detector," presented at the IEEE Room Temperature Semiconductor Devices, Anahiem, CA, October 2012.
[31]P. M. Shikhaliev, T. Xu, and S. Molloi, "Photon counting computed tomography: Concept and initial results," Med. Phys. **32**, 427–436 (2005).
[32]P. M. Shikhaliev, "Tilted angle CZT detector for photon counting/energy weighting x-ray and CT imaging," Phys. Med. Biol. **51**, 4267–4287 (2006).
[33]P. M. Shikhaliev and S. G. Fritz, "Photon counting spectral CT versus conventional CT: Comparative evaluation for breast imaging application," Phys. Med. Biol. **56**, 1905–1930 (2011).
[34]H. Ding, J. L. Ducote, and S. Molloi, "Breast composition measurement with a cadmium-zinc-telluride based spectral computed tomography system," Med. Phys. **39**, 1289–1297 (2012).
[35]C. Szeles, S. Soldner, S. Vydrin, J. Graves, and D. Bale, "CdZnTe semiconductor detectors for spectroscopic x-ray imaging," IEEE Trans. Nucl. Sci. **35**, 572–582 (2008).
[36]D. Bale and C. Szeles, "Nature of polarization in wide-bandgap semiconductor detectors under high-flux irradiation: Application to semi-insulating CdZnTe," Phys. Rev. B **77**, 035205 (2008).
[37]B. Heismann, D. Niederloehner, P. Hackenschmied, M. Strassburg, S. Janssen, and S. Wirth, "Spectral and spatial resolution of semiconductor detectors in medical x- and gamma ray imaging," in *IEEE Nuclear Science Symposium Conference Record* (2008), pp. 78–83.
[38]S. J. Glick, S. Thacker, X. Gong, and B. Liu, "Evaluating the impact of x-ray spectral shape on image quality in flat-panel CT breast imaging," Med. Phys. **34**, 5–24 (2007).
[39]M. Weigel, S. V. Vollmar, and W. A. Kalender, "Spectral optimization for dedicated breast CT," Med. Phys. **38**, 114–124 (2011).
[40]R. L. McKinley, M. P. Tornai, E. Samei, and M. L. Bradshaw, "Simulation study of a quasi-monochromatic beam for x-ray computed mammotomography," Med. Phys. **31**, 800–813 (2004).
[41]F. Salvat, J. Fernandez-Varea, and J. Sempau, "PENELOPE, A Code System for Monte Carlo Simulation of Electrons and Photon Transport (Issy-les-Moulineaux, France: OECD Nuclear Energy Agency, 2003), available in PDF format at http://www.nea.fr.
[42]J. M. Boone, T. R. Fewell, and R. J. Jennings, "Molybdenum, rhodium, and tungsten anode spectral models using interpolating polynomials with application to mammography," Med. Phys. **24**, 1863–1874 (1997).
[43]E. Roessl and R. Proska, "K-edge imaging in x-ray computed tomography using multi-bin photon counting detectors," Phys. Med. Biol. **52**, 4679–4696 (2007).
[44]J. Schlomka, E. Roessl, R. Dorscheid, S. Dill, G. Martens, T. Istel, C. Baumer, C. Herrmann, R. Steadman, G. Zeitler, A. Livne, and R. Proska, "Experimental feasibility of multi-energy photon counting K-edge imaging in pre-clinical computed tomography," Phys. Med. Biol. **53**, 4031–4047 (2008).
[45]J. A. Nelder and R. Mead, "A simplex-method for function minimization," Comput. J. **7**, 308–313 (1965).
[46]R. L. Siddon, "Fast calculation of the exact radiological path for a three-dimensional CT array," Med. Phys. **12**, 252–255 (1985).
[47]S. Thacker and S. J. Glick, "Normalized glandular dose (DgN) coefficients for flat-panel CT breast imaging," Phys. Med. Biol. **49**, 5433–5444 (2004).

[48]P. C. Johns and M. J. Yaffe, "X-ray characterisation of normal and neoplastic breast tissues," Phys. Med. Biol. **32**, 675–695 (1987).
[49]NIST, "Tables of X-Ray Mass Attenuation Coefficients," (2013), http://www.nist.gov/pml/data/xraycoef/.
[50]P. M. Shikhaliev, "Energy-resolved computed tomography: First experimental results," Med. Phys. **53**, 5595–5613 (2008).
[51]G. Knoll, *Radiation Detection and Measurement*, 3rd ed. (Wiley, New York, 2000).
[52]M. Krause, "Atomic radiative and radiationless yields for K and L shells," J. Phys. Chem. Ref. Data **8**, 307–329 (1979).
[53]T. G. Schmidt, "An empirical method for correcting the detector spectral response in energy-resolved CT," in *SPIE Medical Imaging* (San Diego, CA, 2012), Vol. 8313.
[54]S. J. Glick and C. S. Didier, "The effect of characteristic x-rays on the spatial and spectral resolution of a CZT based detector for breast CT," Proc. SPIE Med. Imaging **7961**, 796110 (2011).